

# The carbon distribution in multicrystalline silicon ingots grown using the directional solidification process

Ying-Yang Teng<sup>a</sup>, Jyh-Chen Chen<sup>a,\*</sup>, Chung-Wei Lu<sup>b</sup>, Chi-Yung Chen<sup>c</sup>

<sup>a</sup> National Central University, Taiwan, ROC

<sup>b</sup> Jen-Teh College, Taiwan, ROC

<sup>c</sup> Sino-American Silicon Products Inc., Taiwan, ROC

## ARTICLE INFO

Available online 14 November 2009

### Keywords:

A1. Computer simulation  
A1. Heat transfer  
A1. Impurities  
A1. Mass transfer  
B3. Solar cells

## ABSTRACT

In this study, we performed a numerical simulation of the growth of multicrystalline silicon ingots using the DSS method and compared the results with the experiments. The thermal flow field and the carbon concentration distribution during the growth process were analyzed under the same operating conditions. The carbon concentration distribution in the grown ingots was measured and the results compared with that of the simulation predictions. The simulation results are in good agreement with the experimental ones. The simulation shows that in a directional solidification furnace carbon impurities accumulate easily in the melt near the central region of the melt/crystal interface due to convection. This is the main reason for the non-uniformity of the carbon concentration in ingots grown in the DSS furnace. In order to improve the uniformity of carbon distribution in the melt, a higher convexity of crystalline front interface in the central region needs to be maintained during the growth process to reduce the strength of melt convection around the crystalline front interface.

© 2009 Elsevier B.V. All rights reserved.

## 1. Introduction

Today, the multicrystalline silicon (mc-Si) solar cell has the highest market share of all solar cells in the world. It is well known that the efficiency of an mc-Si solar cell is strongly dependent on the quality of the mc-Si wafers, which are cut from massive mc-Si ingots. The quality of the as-grown ingots is affected by the impurity content and concentration from the feedstock, and the dissolution that occurs in the crucible and heating apparatus during growth [1,2]. One of the major impurities in silicon feedstock is carbon. Pizzini et al. [3] showed that the density and electrical activity of dislocations in an mc-Si ingot is strongly dependent on the carbon concentration [4]. The carbon concentration in the silicon crystal is lower than the one in the silicon melt, because the segregation coefficient of carbon is less than one [4,5]. Silicon carbide (SiC) particles will precipitate as the carbon concentration rises beyond the solubility limit in the silicon melt [4]. Therefore, the carbon content in the silicon feedstock must be kept as low as possible.

Directional solidification (DS) is the most common method for producing the mc-Si ingots in the PV industrial processes. Today,

it is common for companies to produce mc-Si ingots with a weight of 240 kg. Due to the large dimensions of the crucible in the DS furnace, the melt convection generated by the radial temperature gradient forms two coupled vortices in the melt [1,6,7]. Since the diffusion coefficient of impurities in the Si melt is usually very small, the influence of melt convection on the impurity distribution may be significant during directional solidification of mc-Si ingots [8]. Muhlbauer et al. [9] found that the incorporation of the SiC particles in the growing crystal is prevented by the convective melt flow. Liu et al. [4] have investigated the carbon concentration and SiC precipitation during an mc-Si directional solidification process. Their results indicate that the impurities can be controlled by the cooling rate. Manginck-Noel and Duffar [10] showed that impurities can also be reduced by preserving a higher thermal gradient. The grain distribution of the as-grown ingots can be controlled by the modification of the furnace configuration so as to change the evolutionary history of the crystalline front shape [11]. Since the flow convection inside the melt is different for unique crystalline front shapes, we can expect that the carbon distribution in the ingot will be different for unique crystalline front histories.

In this study, a series of numerical simulations are performed to investigate how the convection pattern of the melt affects the carbon concentration distribution during the growth process in a GT-DSS240 furnace. The carbon distribution in the ingots grown in the GT-DSS240 furnace (produced by Sino-American Silicon

\* Corresponding author at. Department of Mechanical Engineering, National Central University, no.300, Jhongda Rd., Jhongli City, Taoyuan County 32001, Taiwan, ROC. Tel.: +886 3 4267321; fax: +886 3 4254501.  
E-mail address: [jcchen@cc.ncu.edu.tw](mailto:jcchen@cc.ncu.edu.tw) (J.-C. Chen).

Products Inc. (SAS)) was measured and the results compared with the numerical ones.

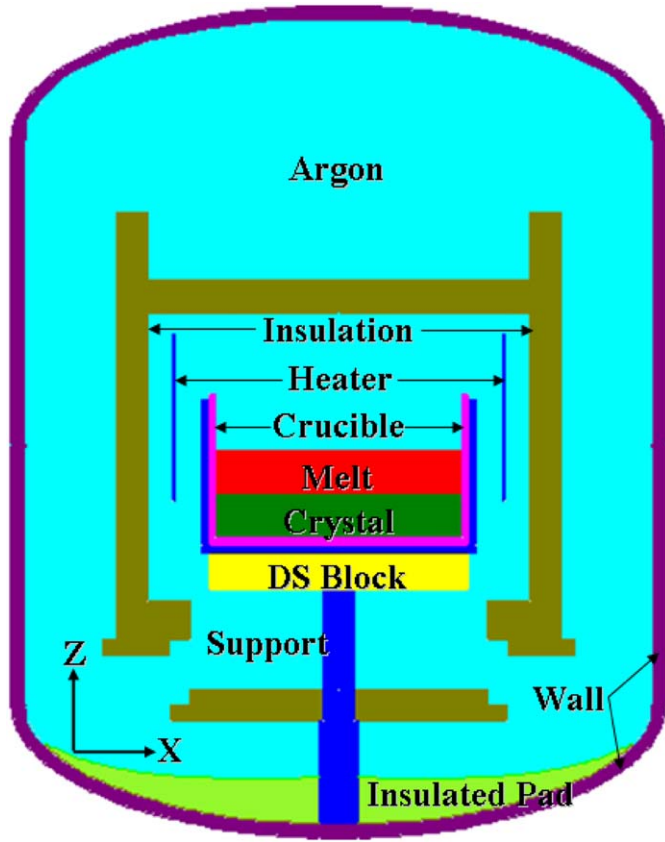


Fig. 1. Schematic diagram of the major components of the DSS furnace.

## 2. Mathematical model

A schematic representation of the industrial DSS furnace used in this study is shown in Fig. 1. The temperature of the furnace wall is kept constant by a cooling system, and the side insulation moves upward during ingot growth. The mc-Si ingot grows from the bottom to the top of the crucible by the dissipation of heat from the bottom of the crucible to the furnace wall.

An axis-symmetric furnace is assumed in the numerical simulation. The melt is assumed to be a Newtonian fluid and the deformation of the free surface is neglected. The buoyancy convection may be generated by the temperature and concentration gradients in the melt. The Lewis number  $Le$ , which is defined as the ratio of the thermal diffusivity  $\alpha$  to the mass diffusivity  $D$ , represents the relative strength of the buoyancy force induced by the non-uniform temperature to that generated by the non-uniform concentration. The Lewis number  $Le$  for the carbon concentration in the silicon melt is about 1000. Therefore, the buoyancy due to the non-uniform concentration can be neglected in the present study. The material properties of silicon are shown in Table 1 [2,8,12,13].

The differential equations governing heat and mass transport are listed as follows:

In the fluid

$$\frac{\partial \rho_i}{\partial t} + \nabla \cdot (\rho_i \vec{u}_i) = 0, \quad (1)$$

$$\frac{\partial (\rho_i \vec{u}_i)}{\partial t} + (\vec{u}_i \cdot \nabla) \rho_i \vec{u}_i = -\nabla p_i + \nabla \cdot \tau_i + (\rho_i - \rho_{i_0}) \cdot \vec{g}, \quad (2)$$

$$\frac{\partial (\rho_i C_{p_i} T_i)}{\partial t} + \rho_i C_{p_i} \vec{u}_i \cdot \nabla T_i = \nabla \cdot (k_i \nabla T_i), \quad (3)$$

$$\frac{\partial (\rho_i \phi_i)}{\partial t} + \nabla \cdot (\rho_i \vec{u}_i \phi_i) = \nabla \cdot (D_{\phi_i} \nabla \phi_i), \quad (4)$$

Table 1  
Physical properties.

Material	Variable	Value
Liquid silicon	Density, $\rho$ (kg/m <sup>3</sup> )	2570
	Specific heat, $C_p$ (J/K kg)	915
	Heat conductivity, $k_i$ (W/Km)	66.5
	Emissivity, $\varepsilon$	0.3
	Melting temperature, $T_m$ (K)	1685
	Latent heat, $\Delta H$ (J/kg)	$1.8 \times 10^6$
	Dynamic viscosity, $\mu$ (Pa s)	$8 \times 10^{-4}$
	$d\sigma/dT$ (N/K m)	$1.5 \times 10^{-4}$
	Diffusion coefficient for carbon, $D_m$ (m <sup>2</sup> /s)	$3 \times 10^{-8}$
Silicon crystal	Density, $\rho$ (kg/m <sup>3</sup> )	2530
	Specific heat, $C_p$ (J/K kg)	1000
	Heat conductivity, $k_c$ (W/Km)	$75(T/300)^{-0.32} \exp(-5.3 \times 10^{-4}(T-300))$
	Emissivity, $\varepsilon$	0.7
	Diffusion coefficient for carbon, $D_c$ (m <sup>2</sup> /s)	$3 \times 10^{-14}$
Quartz	Density, $\rho$ (kg/m <sup>3</sup> )	2650
	Specific heat, $C_p$ (J/K kg)	74
	Heat conductivity, $k$ (W/Km)	4
	Emissivity, $\varepsilon$	0.85
Graphite	Density, $\rho$ (kg/m <sup>3</sup> )	1950
	Specific heat, $C_p$ (J/K kg)	710
	Heat conductivity, $k$ (W/Km)	$105(T/300)^{-0.3} \exp(-3.5 \times 10^{-4}(T-300))$
	Emissivity, $\varepsilon$	0.8
Insulation	Density, $\rho$ (kg/m <sup>3</sup> )	160
	Specific heat, $C_p$ (J/K kg)	100
	Heat conductivity, $k$ (W/Km)	$0.022(T/300)^{-0.14} \exp(-1.05 \times 10^{-3}(T-300))$
	Emissivity, $\varepsilon$	0.7
Argon	Specific heat, $C_p$ (J/K kg)	521
	Heat conductivity, $k$ (W/Km)	$0.01 + 2.5 \times 10^{-5}T$
	Dynamic viscosity, $\mu$ (Pa s)	$8.466 \times 10^{-6} + 5.365 \times 10^{-8}T - 8.682 \times 10^{-12}T^2$
	Gas constant (J/K kmole)	8314

Here,  $t$ ,  $\rho$ ,  $\rho_0$ ,  $C_p$ ,  $\vec{u}$ ,  $T$ ,  $k$ ,  $p$ ,  $\tau$ ,  $\vec{g}$ ,  $\varphi$  and  $D_\varphi$  are the time, density, reference density, heat capacity, velocity vector, temperature, thermal conductivity, pressure, stress tensor, gravitational acceleration, carbon concentration and diffusion coefficient of carbon in the melt, respectively. The subscripts  $i$  may be  $g$  or  $l$ , where  $g$  and  $l$  indicate the gas and melt, respectively. The impurities in the gas domain are not considered in the present study.

The boundary conditions for the fluid velocity at the solid walls are as follows: the normal velocity components at the wall are zero; the tangential velocity component at the wall is equal to the wall velocity. Along the melt–gas interface, the normal velocity component is set to zero and the tangential velocity component has to satisfy the Marangoni condition

$$\mu_l \frac{\partial u_{\tau l}}{\partial n} = \mu_g \frac{\partial u_{\tau g}}{\partial n} + \frac{\partial \sigma}{\partial T} \frac{\partial T}{\partial \tau}, \quad (5)$$

where,  $\mu$  is the dynamics viscosity,  $\tau$  one of the two orthogonal directions tangential to the free surface,  $n$  the normal direction of the free surface, and  $\sigma$  the surface tension of liquid silicon.

In the crystal

$$\frac{\partial(\rho_s C_p T_s)}{\partial t} = \nabla \cdot (k_s \nabla T_s), \quad (6)$$

$$\frac{\partial(\rho_s \varphi_s)}{\partial t} = \nabla \cdot (D_{\varphi_s} \nabla \varphi_s), \quad (7)$$

In the heater

$$\frac{\partial(\rho_h C_p T_h)}{\partial t} = \nabla \cdot (k_h \nabla T_h) + \dot{q}, \quad (8)$$

In the other solid components

$$\frac{\partial(\rho_{si} C_p T_{si})}{\partial t} = \nabla \cdot (k_{si} \nabla T_{si}), \quad (9)$$

Here,  $\dot{q}$  is the heat generation from the heater. The subscripts  $s$ ,  $h$  and  $si$  indicate the crystal, heater and  $i$ th solid component, respectively.

The thermal conditions on the interface between two opaque surfaces are

$$\left( k \frac{\partial T}{\partial n} \right)_1 = \left( k \frac{\partial T}{\partial n} \right)_2, \quad (10)$$

$$T_1 = T_2, \quad (11)$$

The heat fluxes along the interface between the opaque surface and the gas can be expressed as follows:

$$\left( k \frac{\partial T}{\partial n} \right)_{\text{opaque}} = \left( k \frac{\partial T}{\partial n} \right)_{\text{gas}} + \sigma_s \varepsilon T^4 - Q^{\text{in}}, \quad (12)$$

where  $\sigma_s$  is the Stefan–Boltzmann constant,  $\varepsilon$  the emissivity,  $Q^{\text{in}}$  the incoming radiation heat absorbed by the opaque surface.

The temperature at the melt/crystal interface is equal to the melting temperature of silicon, and the energy should satisfy the Stefan condition

$$T = T_{\text{melt}}, \quad (13)$$

$$\rho_s u_n \Delta H = \left( k_l \frac{\partial T}{\partial n} \right)_{\text{melt}} - \left( k_s \frac{\partial T}{\partial n} \right)_{\text{crystal}}, \quad (14)$$

where  $u_n$  is the local crystalline rate normal to the melt–crystal interface and  $\Delta H$  the latent heat.

The zero carbon mass flux is specified at the crucible walls and gas–melt interfaces; the segregation effect is taken into account for carbon impurities. The segregation phenomenon at a melt/crystal interface is described by

$$k_o \varphi_l = \varphi_s, \quad (15)$$

$$D_{\varphi_l} \frac{\partial \varphi_l}{\partial n} + u_n \varphi_l (1 - k_o) = D_{\varphi_s} \frac{\partial \varphi_s}{\partial n}, \quad (16)$$

The segregation coefficient of carbon  $k_o$  is selected to be 0.07 [4].

The energy, continuity, momentum and species equations with proper initial and boundary conditions are solved by the CGSim package, which is based on the Finite Volume Method (FVM). Both unsteady global and local simulations are carried out in this study. The global simulation is mainly used to compute the heat transfer between the different surfaces of the furnace. The heat fluxes along all boundaries obtained from the global model are used for the input heat fluxes in the local model (Fig. 2). In the local model, the heat, flow, mass transfer and the crystalline front are computed iteratively.

### 3. Results and discussion

The unsteady numerical simulation for the growth process of an mc-Si ingot with 69 cm diameter and 24.5 cm height in the standard GT-DSS240 furnace was carried out. Based on the carbon concentration of the feedstock used by the Sino-American Silicon Products Inc. (SAS), the initial carbon concentration  $\varphi_0$  was selected to be 24 ppma. The instant melt flow, temperature, and carbon concentration distributions for different solidification fractions are shown in Figs. 3–7. According to the hot zone characteristic of the standard DSS furnace, the heat is mainly conducted into the melt via the upper crucible side wall and is radiated to the free surface of the melt from the components of the furnace, while the heat is conducted outward by the lower part of crucible side wall and the bottom of the crucible. The latent heat is released into the melt at the melt/crystal interface. Therefore, the maximum temperature of the melt appears at the tri-junction point of the crucible–melt–gas phases. For the case of a 6% solidification fraction, the temperature near the crucible side wall is higher than that near the center region at the same horizontal level in the upper part of the melt region, while it is lower for the melt region near the crystalline front (Fig. 3(a)). The Grashof number  $Gr$  reflects the strength of the buoyancy convection, and the Marangoni number  $Ma$  denotes the magnitude of thermocapillary convection. The order of  $Gr$  ( $10^7 \sim 10^8$ ) is much larger than that of  $Ma$  ( $10^2 \sim 10^3$ ); this

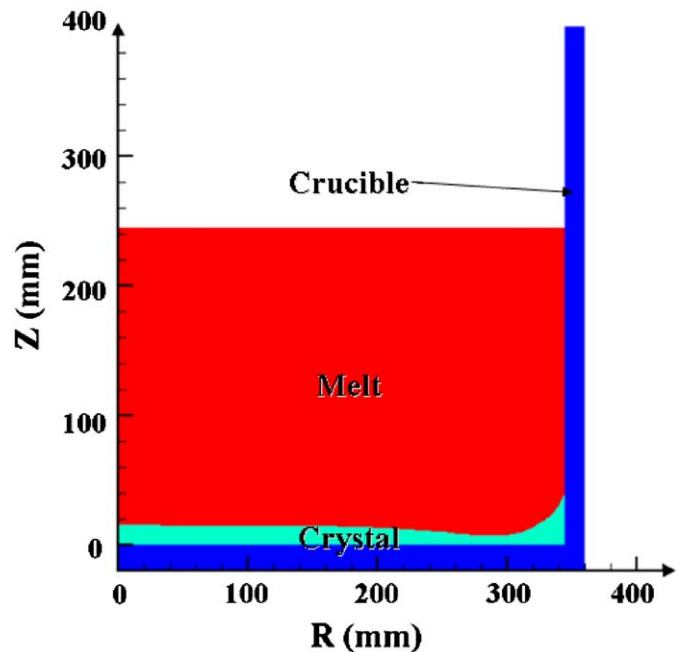
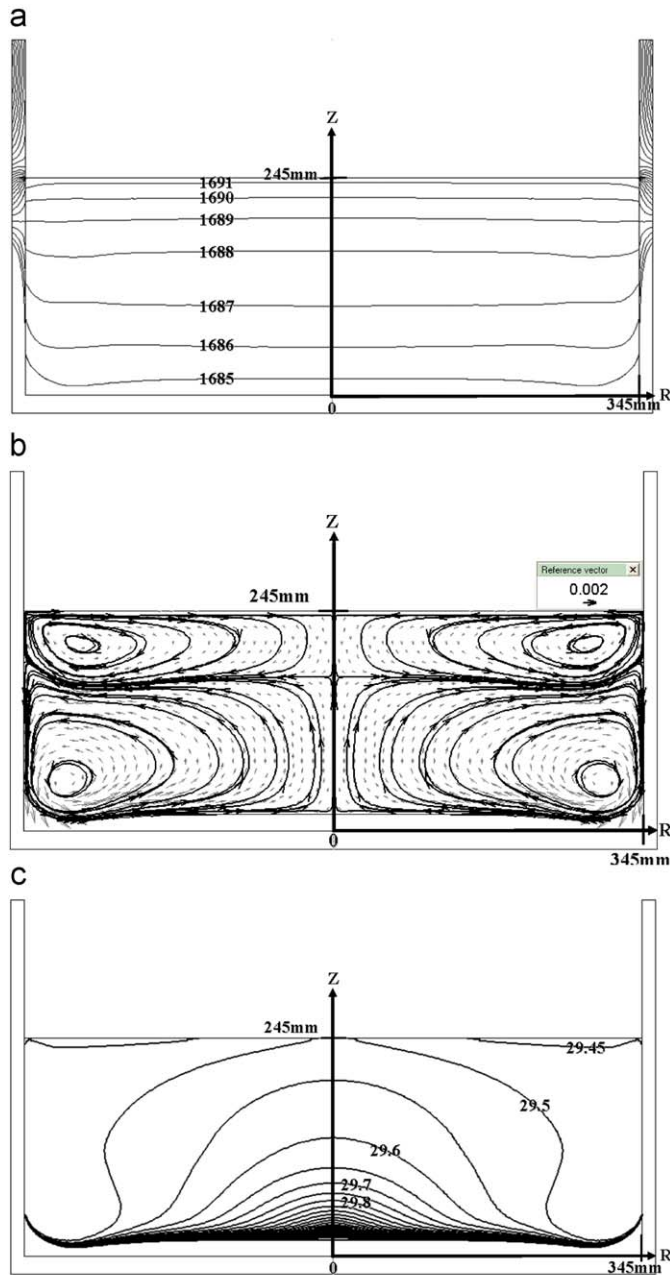


Fig. 2. Schematic diagram of the DSS furnace: local model.

means that the thermocapillary convection is weaker than the buoyancy convection. However, the strength of the buoyancy convection is enhanced by the thermocapillary convection, because the temperature at the crucible is higher than at the center along the free surface. Fig. 3(b) shows the recirculation of the upper vortex generated by both buoyancy and thermocapillary convections circulating inward near the free interface, while the lower vortex induced by the buoyancy force is moving in the opposite direction because of the reversal of the trend of the horizontal temperature. Since the horizontal temperature gradient near the crystal front interface is much higher than that near the free interface, the intensity of the lower vortex is higher than that of the upper one. The maximum

velocity occurs in the lower vortex and the region near the crucible-crystal-melt interface. The Schmidt number, which represents the relative effectiveness of momentum and concentration transport due to diffusion, is approximately 6 for carbon impurities in the silicon melt. Hence, the carbon concentration in the silicon melt is affected by the convection pattern of the silicon melt. Fig. 3(c) displays the carbon distribution in the melt. Carbon impurities in the melt segregate at the crystal front and are carried from the crucible wall to the central region along the crystal front interface, then turned upwards. Since the flow velocity in the central region is smaller in comparison with the others, the upward transport of impurities in the central region is mainly due to diffusion. The impurity



**Fig. 3.** Distribution of temperature, velocity and carbon concentration in the melt for a 6% solidification fraction in the standard DSS furnace: (a) isothermal lines; (b) velocity vector and streamlines; and (c) carbon concentration isolines in the melt. Units of temperature, velocity vector and carbon concentration are K, m/s and ppma, respectively.

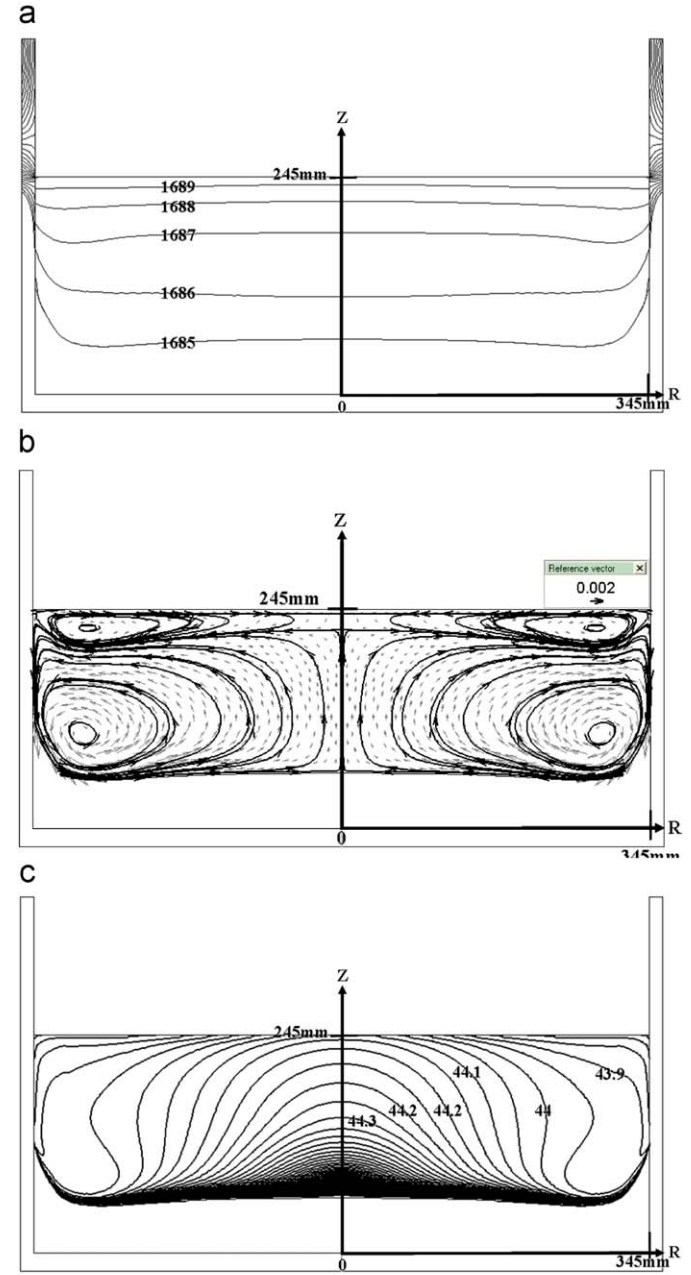


**Fig. 4.** Distribution of temperature, velocity and carbon concentration in the melt for a 29% solidification fraction in the standard DSS furnace: (a) isothermal lines; (b) velocity vector and streamlines; and (c) carbon concentration isolines in the melt. Units of temperature, velocity vector and carbon concentration are K, m/s and ppma, respectively.



transport is enhanced by the upward velocity when the central region nears the crystalline front. The region away from the crystalline front is depressed by the returning flow of the lower vortex and the upcoming flow of the upper vortex. The flow motions near the interface of upper and lower vortices take some impurities away from the central region. The bell shape of carbon concentration isolines in the center region and the stronger distortion of carbon concentration isolines near the crucible wall are generated by the motion of the two coupled vortices. The higher carbon concentration appears at the central region, especially near the crystalline front.

The size and strength of the upper vortex becomes significantly reduced for higher solidification fractions (Figs. 3–7). As the

solidification fraction increases from 6 to 29%, the strength of the lower vortex increases and the carbon concentration isolines near the crucible wall becomes distorted more severely. This occurs due to an increase in the horizontal temperature gradient near the crystalline front interface. When the solidification fraction is higher than 29%, the upper vortex moves gradually towards the corner region of the crucible side wall, and the strength and size of both the upper and lower vortices decrease. When the solidification fraction is 77%, the lower vortex separates into two vortices. The influence of the convection on the carbon concentration becomes weaker. When the solidification fraction is 93%, the carbon impurities are mainly due to diffusion. As the solidification fraction increases, the intensity of the carbon concentration in the melt

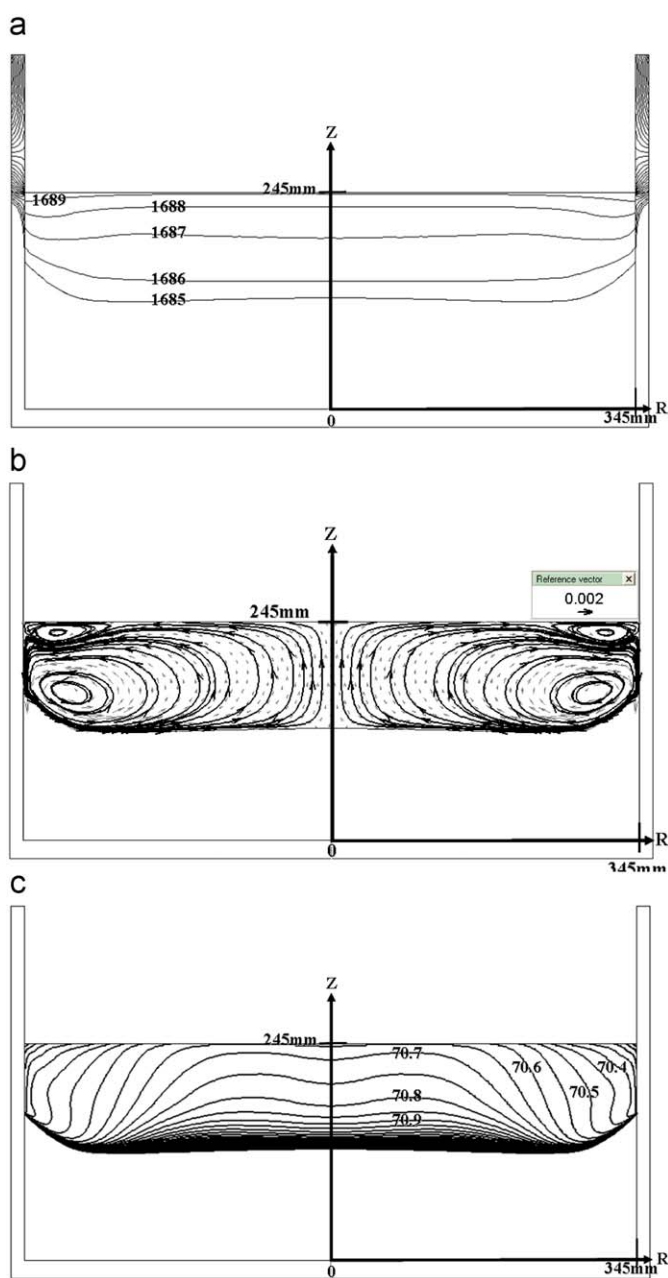


**Fig. 5.** Distribution of temperature, velocity and carbon concentration in the melt for a 56% solidification fraction in the standard DSS furnace: (a) isothermal lines; (b) velocity vector and streamlines; and (c) carbon concentration isolines in the melt. Units of temperature, velocity vector and carbon concentration are K, m/s and ppm, respectively.

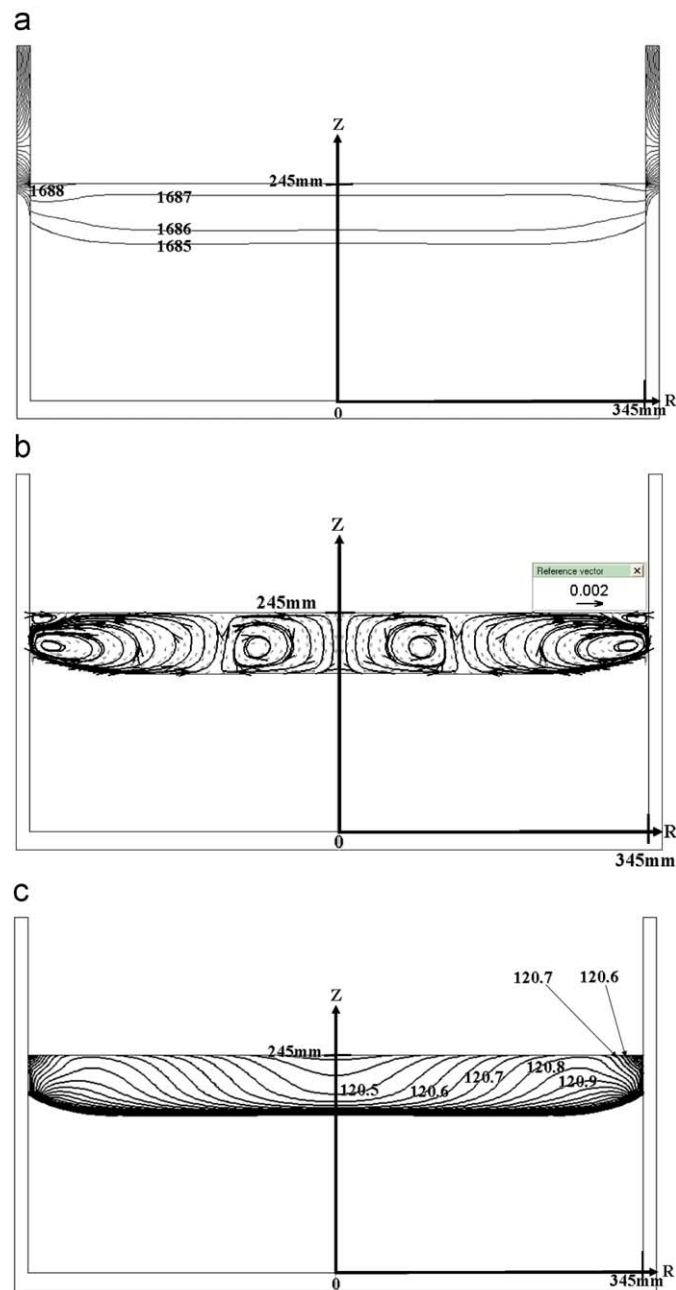


**Fig. 6.** Distribution of temperature, velocity and carbon concentration in the melt for a 77% solidification fraction in the standard DSS furnace: (a) isothermal lines; (b) velocity vector and streamlines; and (c) carbon concentration isolines in the melt. Units of temperature, velocity vector and carbon concentration are K, m/s and ppm, respectively.

increases. This is because the segregation coefficient is much less than one and the locations with higher carbon concentrations usually occur near the center of the crystalline front. When the solidification fraction is greater than 68% the higher carbon concentration region shifts towards the sidewall of the crucible. This occurs because of the separation of the lower vortex.

The simulated crystalline fronts in a standard GT-DSS240 furnace are convex in the central region and concave near the sidewall of the crucible. The concavity increases and the convexity decreases and then increases as the solidification fraction increases [11]. The hot zone of the standard furnace can be adjusted to obtain higher convexity in the central region of the crystalline front during the growth. This can be achieved by increasing the heat conduction from the support, and the radiative transfer from the directional

solidification block (DS block) to the furnace wall. In this way, better grain structure of the ingot is achieved [11], and solar cells made from this/these ingot(s) by the standard cell fabrication process have higher efficiency [14]. The average conversion efficiency of solar cells produced using wafers for the modified case is about 1.8% higher in comparison with that of the standard ones. The temperature, velocity and carbon concentration fields of this modified DSS furnace are shown in Figs. 8–12. For the 6% solidification fraction, the temperature distribution of the modified case is not significantly different from the standard one (Fig. 8). Therefore, the velocity field and the carbon concentration distribution of the two cases is almost the same. When the solidification fraction is larger than 6%, the temperature gradient in the horizontal direction of the lower part of the melt of the

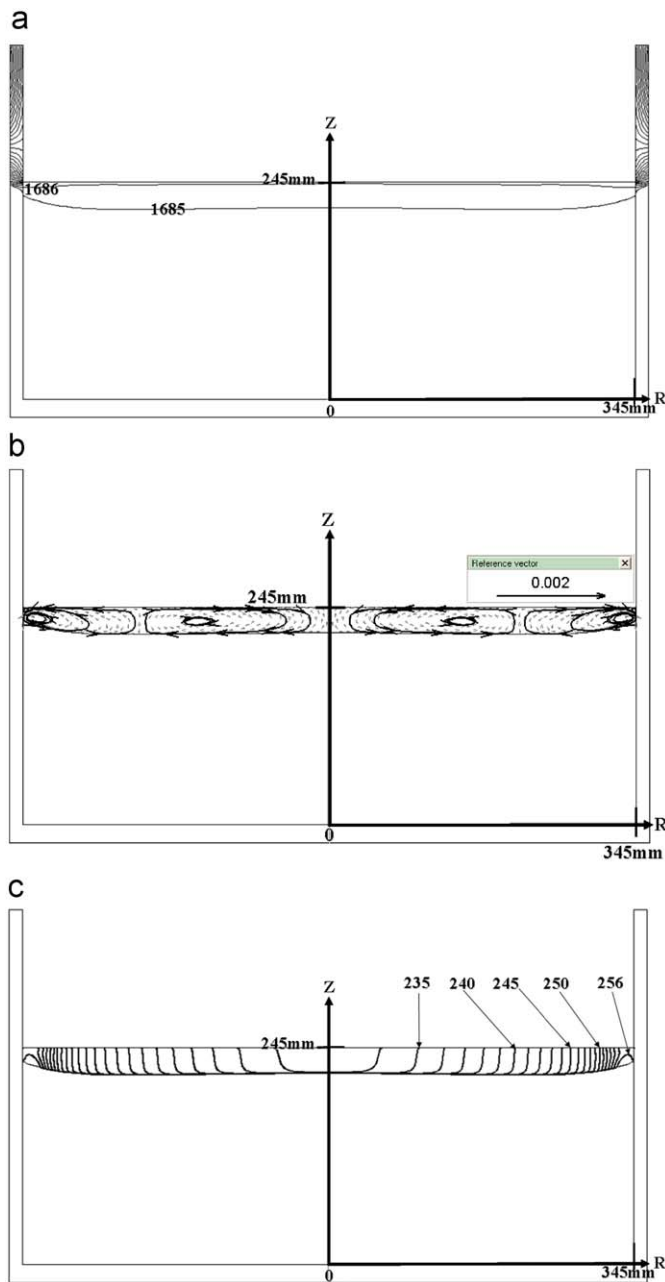


**Fig. 7.** Distribution of temperature, velocity and carbon concentration in the melt for a 93% solidification fraction in the standard DSS furnace: (a) isothermal lines; (b) velocity vector and streamlines; and (c) carbon concentration isolines in the melt. Units of temperature, velocity vector and carbon concentration are K, m/s and ppm, respectively.

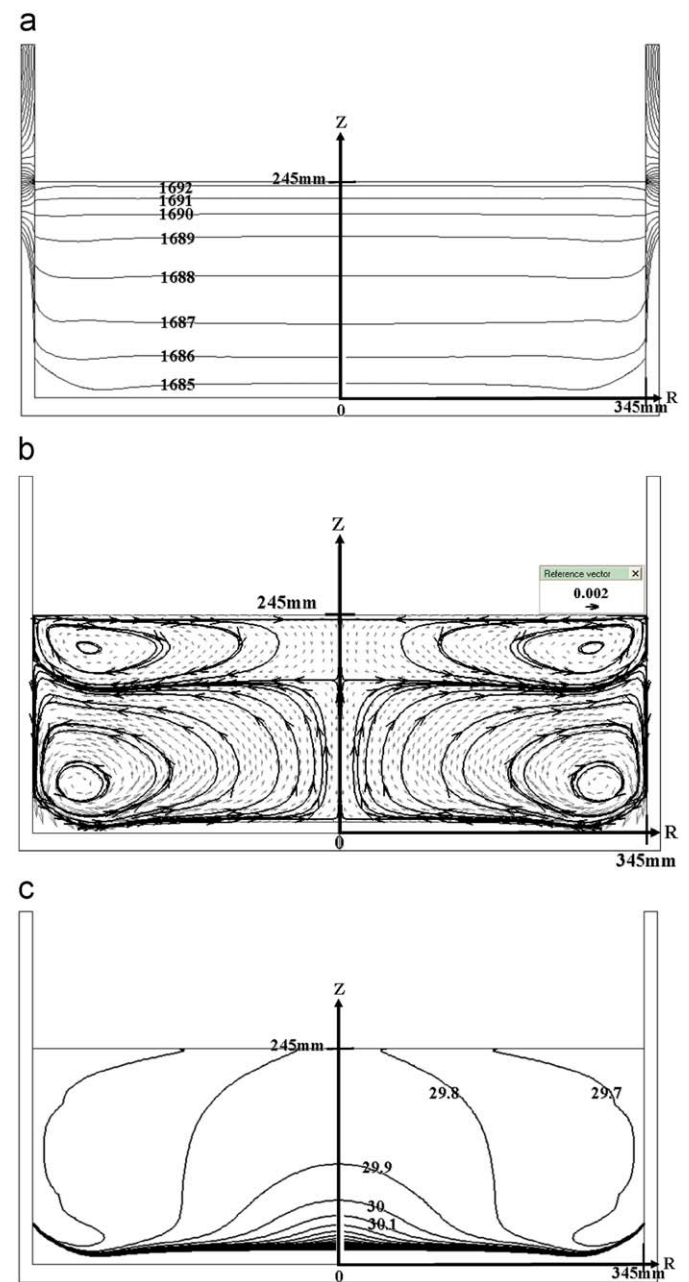


**Fig. 8.** Distribution of temperature, velocity and carbon concentration in the melt for a 6% solidification fraction in the modified DSS furnace: (a) isothermal lines; (b) velocity vector and streamlines; and (c) carbon concentration isolines in the melt. Units of temperature, velocity vector and carbon concentration are K, m/s and ppm, respectively.

modified case is smaller than that of the standard case, and the gradient at the upper part of the melt is higher. The strength of the lower vortex of the modified case is weaker than that of the standard one. In this case it separates into two vortices when the solidification fraction becomes higher than 62%, as opposed to separation at 68% solidification fraction for the standard case. The upper vortex of the modified case is stronger than that of the standard case. The carbon concentration gradients in the melt of the modified case are less than those of the standard ones. Hence, for the modified case, the convection effect of the lower vortex on the carbon concentration is less significant, which may be beneficial to the transverse homogeneity in the carbon distribution. When the solidification fraction is less than 62%, the

maximum carbon concentration in the melt appears at the center. For higher solidification fractions, it occurs near the crucible wall. A rectangular mc-Si ingot with 69 cm width and 24.5 cm height was grown by the standard and modified GT-DSS240 furnace (from Sino-American Silicon products Inc. (SAS)). The carbon concentration of the wafers in the central region of the ingots at different axial positions (for both the modified and standard cases) was measured by FTIR. Fig. 13 shows the variation of carbon concentration with the axial position. The simulation results (both standard and modified cases) are in good agreement with the experimental ones. The average carbon concentration for the modified case is smaller than that for the standard one.

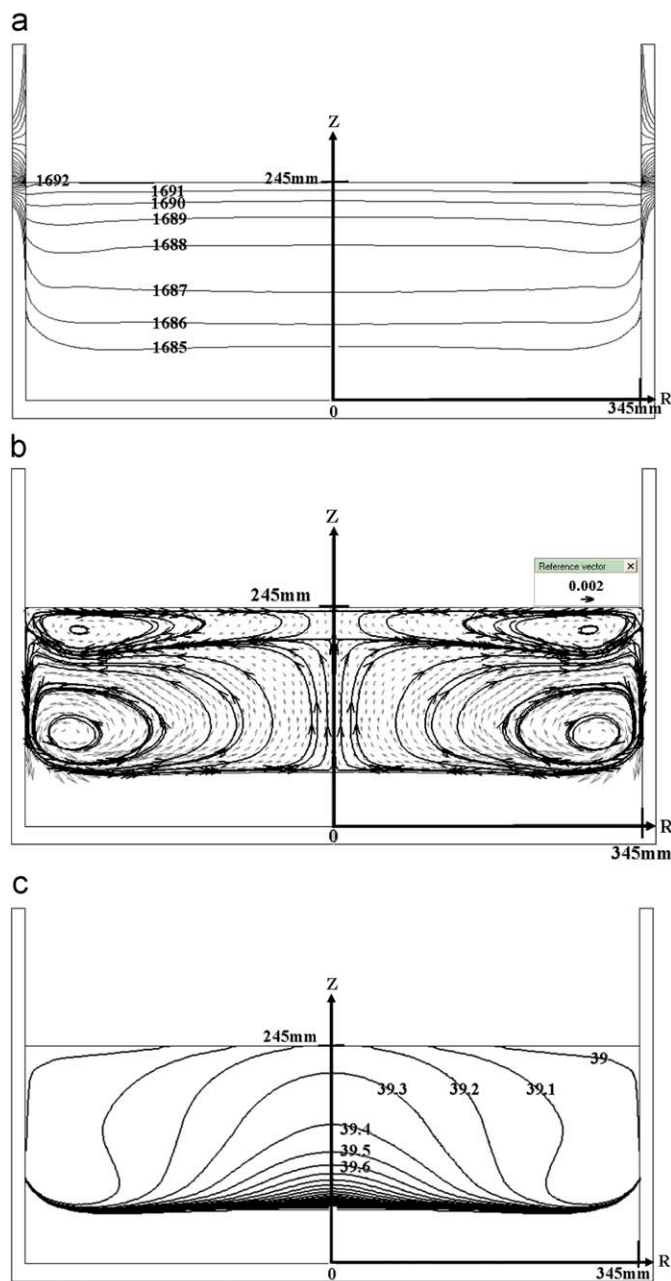


**Fig. 9.** Distribution of temperature, velocity and carbon concentration in the melt for a 29% solidification fraction in the modified DSS furnace: (a) isothermal lines; (b) velocity vector and streamlines; and (c) carbon concentration isolines in the melt. Units of temperature, velocity vector and carbon concentration are K, m/s and ppm, respectively.

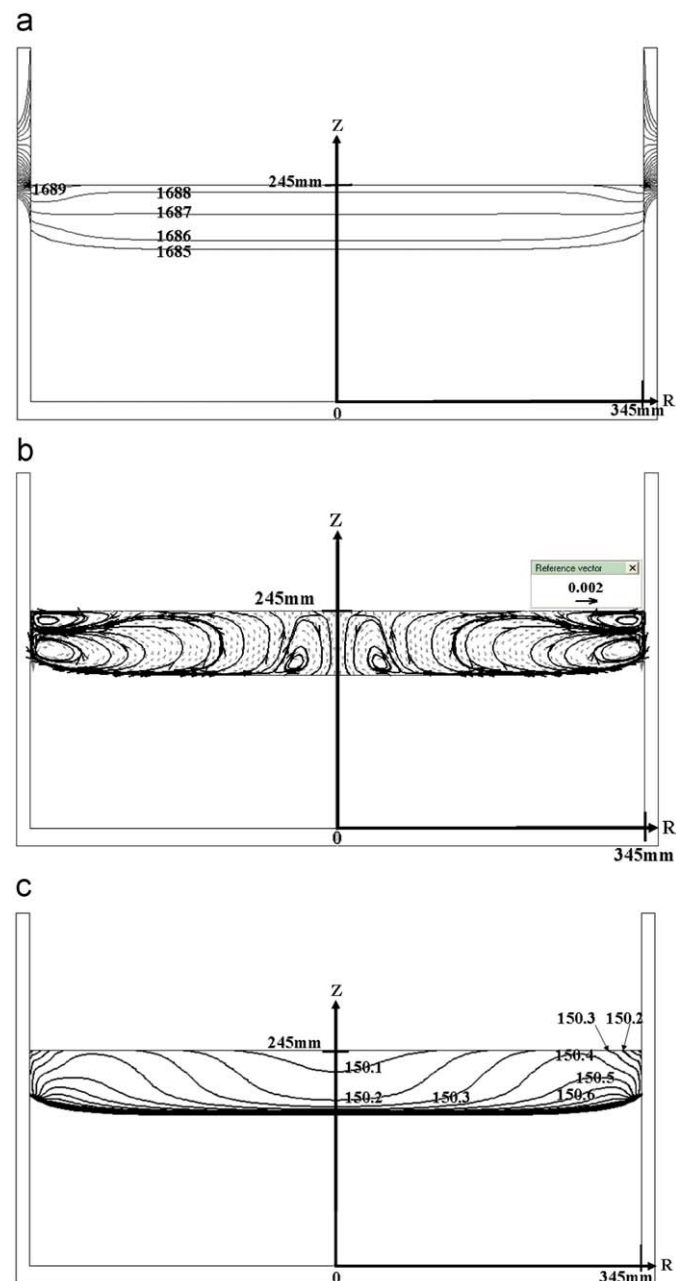


**Fig. 10.** Distribution of temperature, velocity and carbon concentration in the melt for a 56% solidification fraction in the modified DSS furnace: (a) isothermal lines; (b) velocity vector and streamlines; and (c) carbon concentration isolines in the melt. Units of temperature, velocity vector and carbon concentration are K, m/s and ppm, respectively.

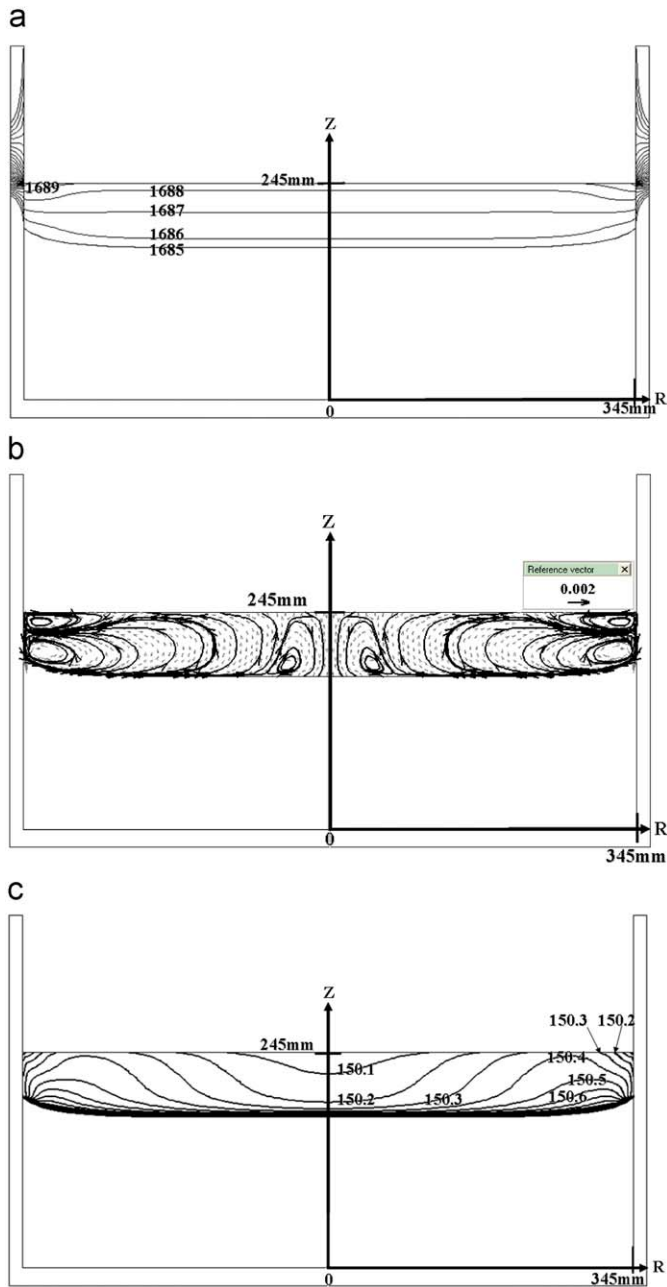


**Fig. 11.** Distribution of temperature, velocity and carbon concentration in the melt for a 77% solidification fraction in the modified DSS furnace: (a) isothermal lines; (b) velocity vector and streamlines; and (c) carbon concentration isolines in the melt. Units of temperature, velocity vector and carbon concentration are K, m/s and ppma, respectively.

#### 4. Conclusion

A simulation of the carbon concentration distribution in the melt during the growth process in an industrial DSS furnace is carried out. Convection is induced in the melt by buoyancy and thermocapillary flow. The vortex pattern in the melt convection changes during the growth process. When the solidification fraction is small, the flow pattern of the melt convection mainly consists of upper and lower vortices coupled to each other. The intensity of the lower vortex is higher than that of the upper one. The motion of the coupled vortices generates bell shaped carbon concentration isolines. At this point a higher carbon concentration appears near the central region of the melt.

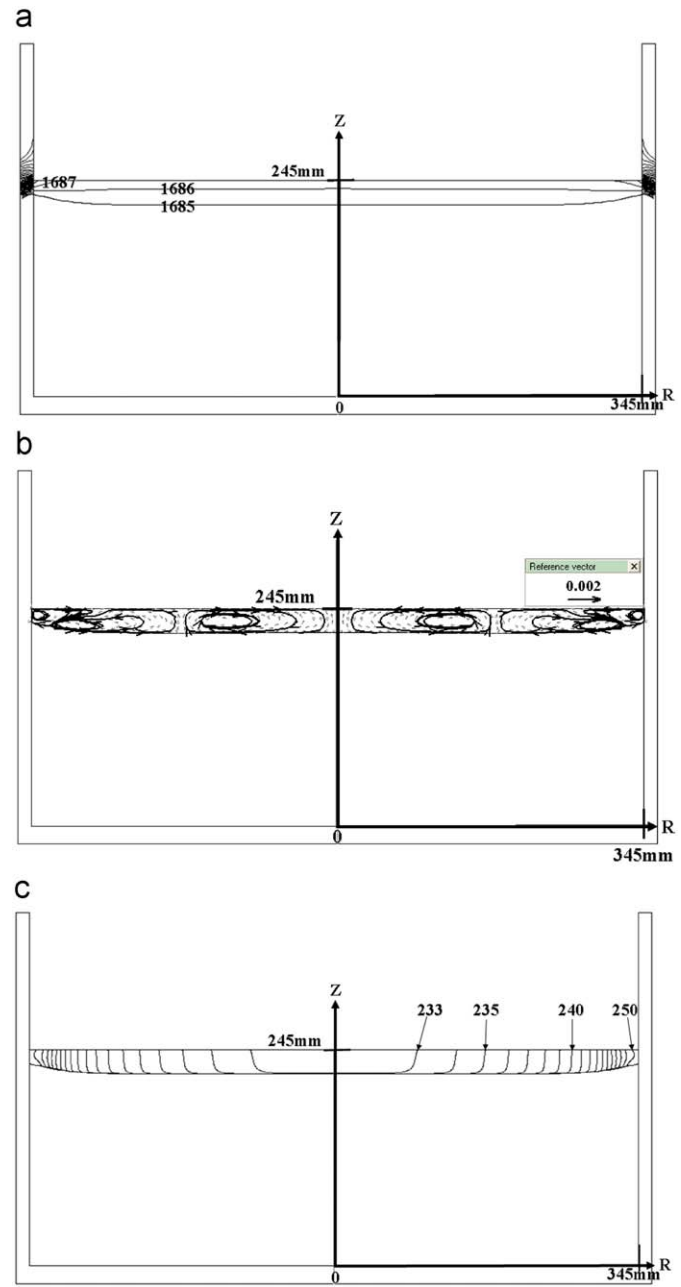


**Fig. 12.** Distribution of temperature, velocity and carbon concentration in the melt for a 93% solidification fraction in the modified DSS furnace: (a) isothermal lines; (b) velocity vector and streamlines; and (c) carbon concentration isolines in the melt. Units of temperature, velocity vector and carbon concentration are K, m/s and ppma, respectively.

When the solidification fraction becomes higher, the upper vortex moves gradually towards the corner region near the crucible side wall and the lower vortex separates into two vortices whose motion induces the higher carbon concentration to move from near the central region of the melt towards the side wall of the crucible.

When the solidification fraction is small the strength of the lower vortex is strong; this is harmful to the homogeneity of the carbon concentration distribution. The large concavity at the central region of the crystalline front increases the strength of the lower vortex. Teng et al. [11] modified the structure of the furnace to obtain higher convexity in the central region of the crystalline front during the growth process. This modification is also



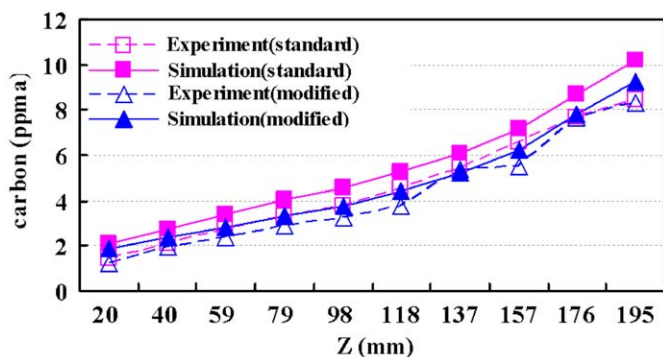


Fig. 13. Variation of average carbon concentration from  $R=0$  to 172.5 mm in the mc-Si ingot along the axial direction with the standard and modified DSS furnaces for the numerical simulation and the experiment.

employed in the present study. With this modified furnace, the strength of the lower vortex is weaker in comparison to the standard one. Both simulation and experimental results show that the average carbon concentration around the center region of the grown ingots is smaller for the modified case than that for the standard one.

### Acknowledgments

The authors would like to thank the National Science Council of Taiwan, ROC, for their support of this work through Grant no. 97-2221-E-008-089-MY3.

### References

[1] A.A. Istratov, T. Buonassisi, M.D. Pickett, M. Heuer, E.R. Weber, Control of metal impurities in dirty multicrystalline silicon for solar cells, *Materials Science and Engineering B* 134 (2006) 282.

[2] P.J. Ribeyron, F. Durand, Oxygen and carbon transfer during solidification of semiconductor grade silicon in different processes, *Journal of Crystal Growth* 210 (2000) 541.

[3] S. Pizzini, A. Sandrinelli, M. Beghi, D. Narducci, F. Allegretti, S. Torchio, G. Fabbri, G.P. Ottaviani, F. Demartin, A. Fusi, Influence of extended defects and native impurities on the electrical properties of directionally solidified polycrystalline silicon, *Journal of The Electrochemical Society* 135 (1) (1988) 155.

[4] Lijun Liu, Satoshi Nakano, Koichi Kakimoto, Carbon concentration and particle precipitation during directional solidification of multicrystalline silicon for solar cells, *Journal of Crystal Growth* 310 (2008) 2192.

[5] Rannveig Kvande, Øyvind Mjos, Birgit Rynningen, Growth rate and impurity distribution in multicrystalline silicon for solar cells, *Materials Science and Engineering A* 413–414 (2005) 545.

[6] Hiroaki Miyazawa, Lijun Liu, Sho Hisamatsu, Koichi Kakimoto, Numerical analysis of influence of tilt of crucibles on interface shape and fields of temperature and velocity in a unidirectional solidification process, *Journal of Crystal Growth* 310 (2008) 1034.

[7] Lijun Liu, Satoshi Nakano, Koichi Kakimoto, Dynamic simulation of temperature and iron distributions in a casting process for crystalline silicon solar cells with a global model, *Journal of Crystal Growth* 292 (2006) 515.

[8] D. Vizman, J. Friedrich, G. Mueller, 3D time-dependent numerical study of the influence of the melt flow on the interface shape in a silicon ingot casting process, *Journal of Crystal Growth* 303 (2007) 231.

[9] A. Muhlbauer, V. Diers, A. Walther, J.G. Grabmaier, Removal of C/SiC from liquid silicon by directional solidification, *Journal of Crystal Growth* 108 (1991) 41.

[10] Nathalie Mangelinck-Noel, Thierry Duffar, Modelling of the transition from a planar faceted front to equiaxed growth: application to photovoltaic polycrystalline silicon, *Journal of Crystal Growth* 311 (2008) 20.

[11] Ying-Yang Teng, Jyh-Chen Chen, Chung-Wei Lu, V.V. Kalaev, S.E. Demina, Crystalline front control of growing multicrystalline Si ingots during the directional solidification process, in: *Proceedings of the 18th International photovoltaic Science and Engineering, PVSEC*, Kolkata, India, January 19–23, 2009.

[12] V.V. Kalaev, D.P. Lukanin, V.A. Zabelin, Yu.N. Makarov, J. Virbulis, E. Dornberger, W. von Ammon, Calculation of bulk defects in CZ Si growth: impact of melt turbulent fluctuations, *Journal of Crystal Growth* 250 (2003) 203.

[13] V.V. Kalaev, I.Yu. Evstratov, Yu N. Makarov, Gas flow effect on global heat transport and melt convection in Czochralski silicon growth, *Journal of Crystal Growth* 249 (2003) 87.

[14] Ying-Yang Teng, Jyh-Chen Chen, Chung-Wei Lu, Chuck Hsu, Chi-Yung Chen, Numerical and experimental study for improving the concavity of the crystalline front in multicrystalline silicone ingots during the directional solidification process, submit to *Solar Energy Material & Solar Cells*.